ADVANCED FUNCTIONAL MATERIALS
www.afm-journal.de

Crystalline CoFeB/Graphite Interfaces for Carbon Spintronics Fabricated by Solid Phase Epitaxy

*P. K. Johnny Wong, Elmer van Geijn, Wen Zhang, Anton A. Starikov, T. Lan Anh Tran, Johnny G. M. Sanderink, Martin H. Siekman, Geert Brocks, Paul J. Kelly, Wilfred G. van der Wiel, and Michel P. de Jong**

Structurally ordered interfaces between ferromagnetic electrodes and graphene or graphite are of great interest for carbon spintronics, since they allow spin-filtering due to k-vector conservation. By solid phase epitaxy of amorphous/nanocrystalline CoFeB at elevated temperatures, the feasibility of fabricating crystalline interfaces between a 3d ferromagnetic alloy and graphite is demonstrated, without suffering from the unwetting problem that was commonly seen in many previous studies with 3d transition metals. The films fabricated on graphite in this way are found to have a strong body-centered-cubic (110) texture, albeit without a unique, well-defined in-plane epitaxial relationship with the substrate lattice. Using various X-ray spectroscopic techniques, it is shown that boron suppresses the formation of CoFe-O during CoFeB deposition, and then diffuses out of the CoFe lattice. Segregation of B occurred exclusively to the film surface upon in situ annealing, and not to the interface between CoFeB and graphite. This is favorable for obtaining a high spin polarization at the hybrid CoFe/graphite crystalline interface. The Co and Fe spin moments in the crystalline film, determined by X-ray magnetic circular dichroism, are found to be bulk-like, while their orbital moments show an unusual giant enhancement which has yet to be understood.

1. Introduction

The young but rapidly growing field of carbon spintronics[1,2] aims to realize spin-based functionalities in carbon-based materials with intrinsically weak spin relaxation and dephasing mechanisms.[3,4] Such features are of very considerable importance for the development of spintronics, since a long spin-lifetime would allow for robust spin manipulation and readout. A particularly interesting example here is graphene, a 2D sheet of carbon atoms with many of its exceptional electronic properties.[5–7] With regard to spintronics, hybrid structures that combine graphene and ferromagnetic materials are basic building blocks. For instance, spin transport in graphene monolayers, bilayers as well as multilayers has already been demonstrated by several groups.[8–13] However, a lack of reliable ways to fabricate clean and structurally ordered ferromagnetic (FM)/graphene interfaces remains a major challenge in this field.[14,15] Karpan et al. have suggested using epitaxial sandwich structures containing Co and/or Ni electrodes separated by multilayer-graphene/graphite.[16] At ideal epitaxial interfaces of Co (or Ni) and graphene/graphite, perfect spin-filtering due to k-vector conservation should be possible in theory, relying on the fact that the only states available at the Fermi energy of graphene/graphite are located or close to the K-points, where there are only minority-spin states from the said ferromagnets.[16] However, a key issue to be tackled is the practical realization of an epitaxial ferromagnetic electrode on top of graphene/graphite. Due to the large difference in surface energy of 3d FM metals and carbon-based materials, FM metals deposited onto graphene/graphite usually exhibit a 3D growth mode.[17–19] This results in poor epitaxy, unless strongly out-of-equilibrium conditions are used.

Recently, the spintronics community has begun to appreciate the technological importance of (initially) amorphous ferromagnetic (a-FM) alloys[20] for achieving novel spin-dependent phenomena relying on lattice-matched interfaces. For instance, magnetic tunnel junctions (MTJs) incorporating the ternary alloy CoFeB in conjunction with an MgO barrier exhibit giant tunneling magnetoresistance values at room temperature (RT).[21,22] The primary mechanism governing this effect is based on the band structure symmetry and the requisite coherent (001)-textured body centered cubic (bcc) crystal structure involved at the CoFeB/MgO interface.[23] Additionally, a-FM alloys feature many desirable properties,[24] such as magnetic

Dr. P. K. J. Wong, E. van Geijn, Dr. W. Zhang, T. L. A. Tran, J. G. M. Sanderink, M. H. Siekman, Prof. W. G. van der Wiel, Dr. M. P. de Jong
NanoElectronics Group
MESA+ Institute for Nanotechnology
University of Twente
P.O. Box 217, 7500 AE, Enschede, The Netherlands
E-mail: M.P.deJong@utwente.nl
A. A. Starikov, Dr. G. Brocks, Prof. P. J. Kelly
Faculty of Science and Technology
MESA+ Insitute for Nanotechnology
University of Twente
P.O. Box 217, 7500 AE, Enschede, The Netherlands

DOI: 10.1002/adfm.201203460

softness due to their amorphous/nanocrystalline nature and tunability of their electronic, magnetic and structural properties by varying elemental compositions, which makes them unquestionably important materials for spintronic applications.

In this paper, we demonstrate the first experimental investigation into the use of CoFeB for fabricating crystalline interfaces with graphite for carbon-based spintronics. Incorporation of an a-FM alloy as the top electrode material on graphite/graphene enables studies on the aforementioned spin-filtering effect at FM/graphene interfaces. The main idea behind our approach is to induce a crystalline interface between the two dissimilar materials by solid phase epitaxy driven by post-deposition annealing, where the a-FM alloy crystallizes at the heterointerface. Consequently, the requirements posed by lattice-matching and surface energy compatibility for epitaxial growth of FM metals on graphene/graphite should be less stringent in this case. It should be noted that this approach is entirely new in relation with carbon-based spintronics, since both the use of a-FM alloys and their interfaces with graphene/graphite have never been reported. Major questions that need to be addressed are the interface crystallinity that can be achieved on the graphene/graphite surfaces, the diffusion mechanisms involved in the annealing induced crystallization, and the electronic and magnetic structure of the hybrid interfaces after the crystallization. By using various X-ray techniques, including X-ray photoelectron spectroscopy (XPS), X-ray diffraction (XRD), synchrotron radiation-based photoelectron spectroscopy (PES), X-ray absorption spectroscopy (XAS), and X-ray magnetic circular dichroism (XMCD), we offer answers to these issues.

2. Results and Discussion

2.1. Surface Structural Properties and Valence Band Electronic Structure of CoFeB/Graphite

Figure 1a–c show a series of low-energy electron diffraction (LEED) patterns capturing the surface structure of CoFeB on highly oriented pyrolytic graphite (HOPG) at different stages of the fabrication process. A clean HOPG surface was obtained by in situ peeling followed by annealing at 550 °C for 60 min. The ring structure (Figure 1a) is characteristic of the in-plane periodicity with random azimuthal orientation of the graphite crystallites. For CoFeB in the as-deposited state, the ring pattern of the HOPG has been completely washed out, and the lack of any identifiable pattern strongly supports the amorphous/nanocrystalline nature of the CoFeB film. Subjecting the magnetic film to thermal annealing at 400 °C for 60 min does not produce any observable change in the LEED pattern. At first glance, this result might lead to the following speculations: (i) the annealed CoFeB remains mostly amorphous in the entire film, which is contrary to the received wisdom about thermal-driven crystallization due to B-diffusion out of CoFeB, (ii) the crystallization of the film is incomplete, leaving its surface amorphous, or (iii) the annealed film crystallizes into a polycrystalline structure without any preferred orientation.

We begin by addressing whether there was B-diffusion upon annealing at the temperature used. The solid and dotted

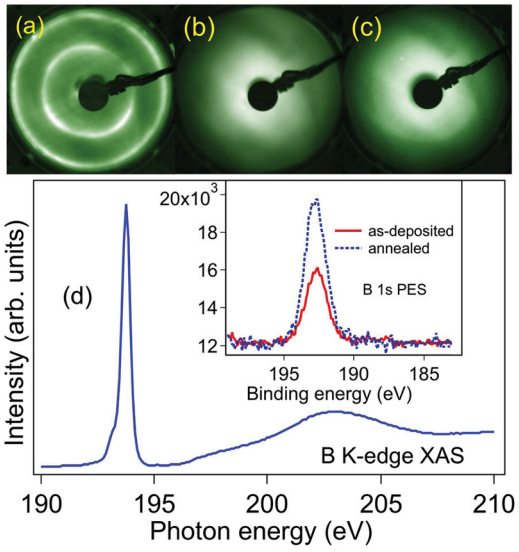

Figure 1. LEED images of a) clean HOPG, electron energy 194 eV; b) As-deposited CoFeB, electron energy 233 eV; c) Annealed CoFeB, electron energy 233 eV. d) B K-edge XAS spectrum. Inset: B 1s PES signal measured with photon energy $h\nu$ = 400 eV before and after annealing.

spectra in the inset of Figure 1d correspond, respectively, to the B 1s peaks of the as-deposited and annealed CoFeB films measured by PES. The significant increase of the B 1s intensity after annealing implies B enrichment of the film surface and hence demonstrates B-diffusion, the principal mechanism of solid phase epitaxy in CoFeB films. However, it is noteworthy that, unlike metallic B, the binding energy of the observed B peak indicates B-O chemical bonds. PES measurements show that the samples indeed contain a small amount of oxygen. In addition, the B K-edge XAS spectrum of the annealed CoFeB/HOPG sample, shown in Figure 1d, also confirms the formation of boron oxide.[25] The overall line shape, the strong resonance at 193.95 eV, and the broad feature at 202.5 eV resemble the spectral features of B_2O_3 very well. According to this interpretation, the strong resonance refers to transitions of B 1s electrons to the unoccupied π^*2p_z molecular orbital of the BO_3^{3-} anion, while the broad feature is due to a shape resonance involving $\sigma^*2p_{x,y}$ molecular orbitals.[25] This boron oxide may stem from the contamination by dissociated O ions from the Al_2O_3 crucible or from the sintered CoFeB source itself during the deposition or both. However, we emphasize that there was no evidence of Co-O or Fe-O chemical bonds, neither in the PES spectra of the Co- and Fe 2p core levels nor in the XAS spectra of the Co- and Fe L-edges. The preferential oxidation of B in CoFeB films has also been recently reported by Han et al.,[26] and can be understood by the stronger oxygen affinity of B compared to Co and Fe.[27,28] From the above, we conclude that the lack of surface crystalline structure in the LEED pattern may be attributed to the formation of amorphous/polycrystalline boron oxide on the CoFeB/HOPG surface.

Due to the low solubility of B atoms in the CoFe matrix (<1%), the crystallization process triggered by annealing requires the rejection of B atoms, which would in turn disturb the Co-B and Fe-B chemical bonds in a given CoFeB film. An interesting aspect

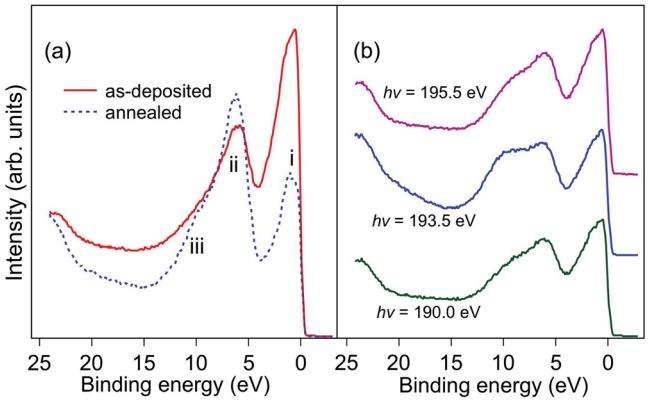

Figure 2. a) The valence band electronic structure of CoFeB measured at normal emission (45° incidence) with photon energy $h\nu = 110$ eV. b) Resonant PES spectra of the valence band region of annealed CoFeB measured with different photon energies across the B 1s absorption edge at normal incidence.

to be investigated in this regard would be the associated modifications in the valence electronic structure of the magnetic layer upon crystallization. In **Figure 2**a, we show that there are indeed pronounced changes in the valence band of CoFeB/HOPG before and after annealing. In the spectra, several features, labeled as i-iii, can be identified. The sharp peak near the Fermi level E_F (feature i) is derived from Co and Fe 3d bands, which, in the case of CoFeB, are affected by the hybridization with the B 2p states.[26,29] Feature ii is assigned to O 2p states due to the presence of a small amount of oxygen contamination on the sample surface, which has been already described. The B 2p states contribute to feature iii, which is not clearly resolved in the as-deposited film.[25] Two spectral changes are observed after annealing, namely, 1) the maximum intensity of feature i shifts slightly to higher binding energy, and 2) the relative intensity ratio of feature i and ii changes considerably. A recent density functional theory calculation has shown that the total- and spin-resolved density of states in bcc-Fe with and without B impurities exhibit different peak positions below the Fermi energy, which has been experimentally verified.[26] Our experimental observation is in very good agreement with these studies and supports the change in the Co-B and Fe-B bands before and after the crystallization process. Note that the overall intensity decrease in the annealed spectrum is ascribed to the out-diffusion of B, consistent with the increase in the intensity of the B 1s spectra in Figure 1d and with the evolved shoulder due to B 2p states, marked by feature iii. The latter is further supported by the photon energy dependence of the CoFeB valence band spectra across the B K-edge as illustrated in Figure 2b. The energies are chosen around the B 1s to π^*2p_z resonance. The on-resonance spectrum at 193.5 eV exhibits a stronger shoulder, whereas off-resonance spectra recorded at 190 eV and 195.5 eV, before and after the π^* peak, respectively, look quite similar both in shape and intensity.

2.2. B Distribution and CoFeB/Graphite Crystallinity

So far, the results presented in the previous section mainly concern the chemical and electronic properties of CoFeB/HOPG

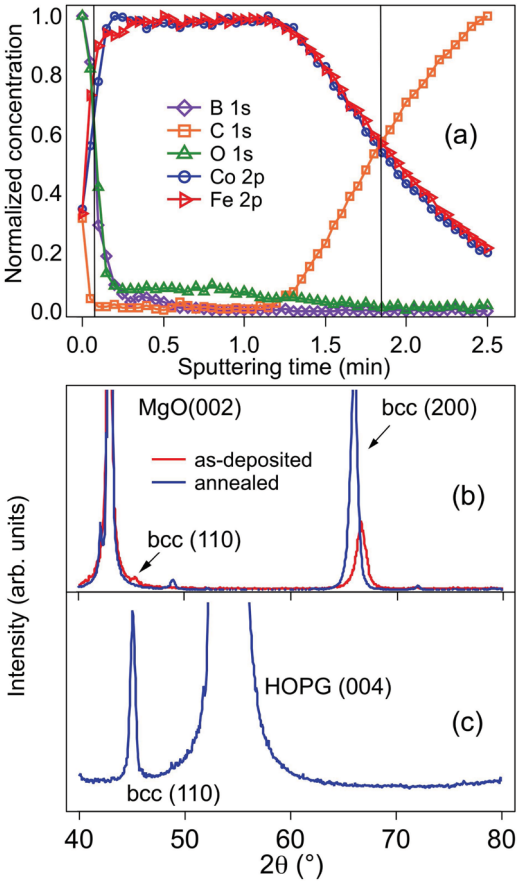

Figure 3. a) Normalized XPS elemental depth profile of CoFeB/HOPG annealed at 400 °C for 60 min. Solid vertical lines indicate the approximate interface positions within the nominal layer structure. B is present mainly at the surface of the magnetic film. b, c) X-ray diffraction patterns of a CoFeB/MgO(001) reference sample and annealed CoFeB/HOPG.

and do not offer much information on the crystallization of the ferromagnetic film. In addition, another key issue that needs to be clarified further is the distribution of B atoms, and in particular the possible accumulation of B at the CoFeB/graphene (or graphite) interface, where the addition of B is detrimental to the proposed spin-filtering effect. **Figure 3**a shows the XPS depth profile of an annealed (30 nm) CoFeB/HOPG sample. The sample was sputtered by using a focused Ar^+ beam of 1 kV on a 3×3 mm^2 window. Characteristic peaks for each elemental species in the sample were recorded at each point in the depth profile. A trace of each elemental species contained within the stack shows the concentration (at%) at a given depth, normalized on the maximum concentration of that species for ease of comparison. Concentrations are extracted from the data after subtraction of a Shirley background and taking into account the corresponding atomic sensitivity factors, which were corrected for the transmission function of the analyzer. Interface broadening in XPS depth profiling is predominantly due to a combination of sampling depth and etch non-uniformity. The intense C 1s and O 1s signals at the initial stage of the sputtering process are due to surface contamination originating from exposure to air. Most importantly, in agreement with the

PES data discussed above, we see that B accumulation exists exclusively on the surface of the magnetic layer, but not at the CoFeB/HOPG interface after the annealing. In accordance, we speculate that the crystallization starts from the hybrid interface, and pushes the B atoms to diffuse upward. It should be noted that the absence of any C signal before the decline of the Co- and Fe signals demonstrates that unwetting between CoFeB and graphite does not occur.

The crystal structure of relatively thick CoFeB films (30 nm) on HOPG before and after annealing was analyzed by θ–2θ XRD. The XRD patterns of similar CoFeB films deposited onto MgO(100) are also shown for comparison in Figure 3b. Besides the high level of intensity from the MgO(100) substrate, we could identify non-negligible bcc-CoFe(110) and (200) peaks prior to the thermal treatment, thus implying that there are traces of crystallites coexisting with the amorphous matrix, due to the relatively low B at% adopted in this study. Nevertheless, the annealed film on MgO becomes highly crystalline with a strong bcc(100) texture, in agreement with extensive studies on MgO-based MTJs.[21,22,30] The shift of the bcc(200) peak to a lower angle upon annealing suggests a change of lattice spacing, probably due to the B out-diffusion from the CoFe lattice. Incorporation of B, with a small ionic radius, into CoFe crystallites might result in a smaller lattice parameter, consistent with Vegard's law. Taking into account the X-ray source wavelength used and the 2θ values in the XRD spectra, we estimated the distance between the atomic layers of the bcc-CoFe{100} planes as 1.402 Å and 1.414 Å for the as-deposited and annealed film, respectively, using Bragg's law. Accordingly, the lattice constant for the former is 2.804 Å, and 2.828 Å for the latter. Notice that the lattice parameter for the annealed case is very close to that of bulk CoFe.[31] Some additional weak signals have not been indexed and could be due to a small fraction of grains with a different texture and/or the presence of an additional minority phase due to surface oxidation. In sharp contrast to the MgO(100) case, the annealed CoFeB/HOPG XRD pattern in Figure 3c reveals a bcc(110) texture. Note that according to the phase diagram of bulk binary Co_xFe_{1-x} alloys, one would expect a stable bcc phase for x lying between 29–70% and an fcc structure when reaching 90%,[32] such that our finding of a bcc(110) texture for CoFeB with nominal composition $Co_{72}Fe_{20}B_8$ is not surprising, but also not expected a priori. The crystalline coherence length of the CoFeB films on both substrates has been computed using the full-width at half maximum of the 2θ graphs according to the Scherrer equation. The results are summarized in **Table 1**. The crystal grains within the as-deposited CoFeB film on MgO(100) are with an out-of-plane dimension of 18 nm. After annealing, the grain size increases by ≈40% to 25 nm, which is comparable with that found for the film deposited on HOPG. It has been shown

Table 1. Crystalline coherence length of CoFeB films on MgO and HOPG.

	Crystalline coherence length [nm]
CoFeB/MgO as-deposited	18
CoFeB/MgO annealed	25
CoFeB/HOPG annealed	26

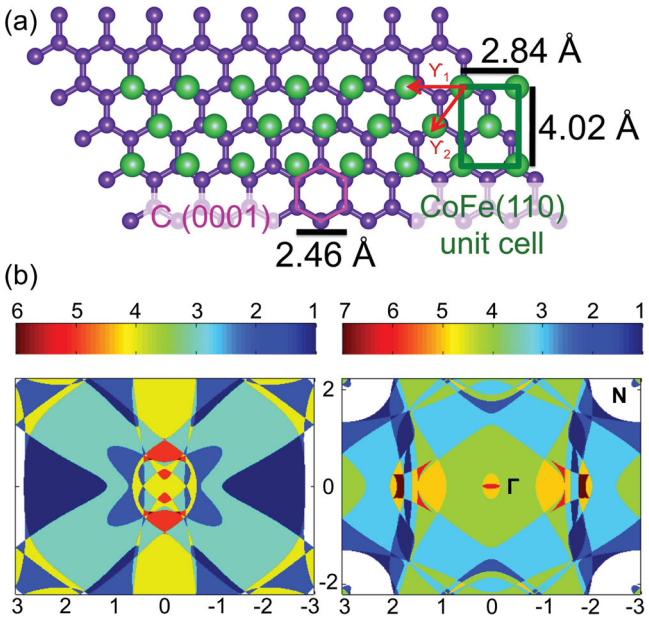

Figure 4. a) Top view of a ball-and-stick model of CoFe(110)/HOPG. The corresponding C hexagon and CoFe(110) unit cell are marked, respectively, by (pink) hexagon and (green) rectangle. Six CoFe(110) units are required to fit seven hexagons of graphene along γ_1, while there exists an almost perfect lattice matching along γ_2. b) Projection of Fermi surfaces of bcc-Co minority- (left) and majority-spin (right) onto (110) plane. The number of Fermi surface sheets is shown by the color bar, and the high symmetry points (Γ and N) of the CoFe(110) unit cell in reciprocal space are also shown.

previously by Takeuchi et al. that the dimension of CoFeB grains on MgO(100) along the growth direction is mainly limited by the film thickness.[33] The grains of CoFeB quantified in the table probably have (almost) reached their maximal sizes, given the film thickness of 30 nm.

Concerning elemental ferromagnetic 3d transition metals, the lattice constants of hexagonal close-packed (hcp)-Co(0001) and face centered cubic (fcc)-Ni(111) surfaces match the in-plane lattice constants of C(0001) almost perfectly (lattice mismatch γ <2%). For bcc-CoFe, the (110) orientation matches C(0001) much better than the (100) and (111) planes. As schematically illustrated in **Figure 4**a, the atomic arrangement of CoFe(110) on HOPG is such that seven parts of the HOPG lattice match six parts of the CoFe(110) lattice. The interfacial spin-filtering effect proposed by Karpan et al. essentially builds from two prerequisites: 1) the lattice matching of FM and graphene, and 2) the minority-spin only character of the FM bands at E_F at graphene's high symmetry K-point.[16] It follows that both of these requirements have to be strictly fulfilled in order to achieve this effect perfectly. In the following, we will comment on the suitability of utilizing our crystalline CoFeB(110)/graphite interface as the spin filter. As already shown in Figure 4a, in order to attain the best possible lattice matching between the FM alloy and surface graphene, the atomic arrangement is such that the CoFe(110) unit cell fits almost perfectly the C hexagon on one direction (γ_2 < 1%, see Figure 4a) and 6 units for 7 of that of graphene on the other (γ_1≈1%). From a crystallographic viewpoint, this configuration

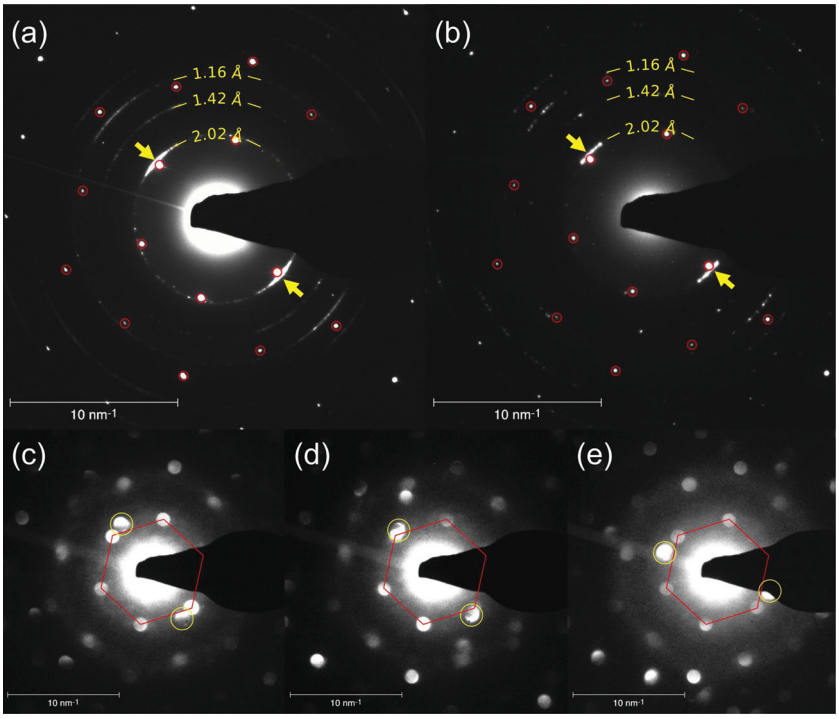

Figure 5. SAED patterns of a representative crystallized 12 nm CoFeB/graphite sample. a) and b) show the patterns obtained on different locations on the sample, using an electron beam radius of ≈100 nm. The red circles refer to the hexagonal diffraction patterns of the graphite lattice, while the numbers in yellow indicate those of the crystallized CoFe. The yellow arrows mark the high intensity regions in the CoFe diffractions. c–e) were captured at different areas of the same sample with a much smaller beam spot (<10 nm diameter). It can be seen that spots belonging to the CoFe (within the yellow circles) are observed at different locations with respect to the diffraction spots of graphite (indicated by the red hexagons).

appears to be less ideal than the case of (111) Co or Ni on graphene, where a hexagon-on-hexagon registry is possible, and may, therefore, induce a symmetry-lowering factor which is likely to decrease the robustness of the spin-filtering effect. We have estimated the degree of such an effect by also considering the band matching between CoFe(110) and graphene. With the presented atomic arrangement, the second prerequisite elaborated by Karpan et al. should be valid for regions where the K-point of graphene/graphite either directly meets or is nearby the N-point of CoFe(110). For simplicity, we show in Figure 4b the spin-resolved Fermi surfaces of bcc-Co projected onto the (110) plane, where an imbalance of minority- versus majority-spin states at the N-point in reciprocal space of Co(110) can be observed. Further taking into account the presence of Fe in the alloy, which features a complicated structure of majority- and minority-spin states at the E_F,[34] the spin-filtering effect and thus the difference in conductance between the parallel and anti-parallel cases in a sandwich structure involving the CoFe(110)/graphene interfaces is estimated to be fairly low. Consequently, at the crystalline CoFe(110)/graphite interface fabricated by solid phase epitaxy, the stringent requirements for the spin filtering are partially fulfilled, meaning that any spin-dependent signal that is mediated by minority-spin transport of CoFe via the K-point of graphene/graphite will be unfavorably affected by the effects caused by the non-ideal atomic registry between CoFe(110) and graphene. One would, however, expect a finite, albeit small, spin-filtering at the fabricated crystalline interface.

In order to verify whether an in-plane epitaxial relationship between crystallized CoFeB and graphite indeed exists, transmission electron microscopy (TEM) and selected area electron diffraction (SAED) have been used. **Figure 5** show a series of SAED patterns obtained from a representative (12 nm) CoFeB film on peeled HOPG (see Supporting Information for details on sample preparation), where diffraction from both materials can be observed. The diffraction patterns recorded on different locations on the same sample using an electron beam radius of ≈100 nm, which probes multiple crystal grains, are illustrated in Figure 5a,b. The red circles refer to the hexagonal patterns of the graphite lattice (with lattice plane spacings of 2.13 Å for the innermost hexagon and 1.23 Å for the subsequent hexagon), while the numbers in yellow indicate the measured lattice plane spacings belonging to the CoFe. The existence of high-intensity regions in the CoFe diffraction pattern clearly indicate a non-random in-plane orientation of the CoFe film. However, one cannot single out a unique epitaxial relationship between the materials either. We have also captured the SAED patterns at different areas of the same sample with a much smaller beam spot of nm diameter, as in Figure 5c–e. For such a small spot size, the patterns are no longer sharp, but individual CoFe grains can be probed resulting in well-defined diffraction spots. As shown, spots that are due to CoFe (within the yellow circles) are observed at different locations with respect to the diffraction spots of graphite, as indicated by the red hexagaons. The locations at which the CoFe spots are observed match well with the high-intensity regions in the large-area SAED patterns. It can thus be concluded that the annealed CoFeB film is, strictly speaking, textured, and lacks a unique in-plane epitaxial relationship with graphite. However, the SAED measurements indicate a non-random in-plane orientation. We attribute these findings to 1) a rather weak but non-negligible interaction between the graphite surface and CoFe, and 2) the poor match between the CoFe(110) and graphite(0001) planes. The implications for the suitability of this particular materials combination as a spin filter are that the filtering efficiency will be deteriorated by the coexistence of many different in-plane orientations of the CoFe crystals on the graphite lattice.

2.3. Magnetic Properties of CoFeB/Graphite by Element-Specific XMCD

XAS and XMCD have been particularly chosen for the present studies, due to their element-specificity and ability to allow for direct and separate quantitative determination of atomic spin

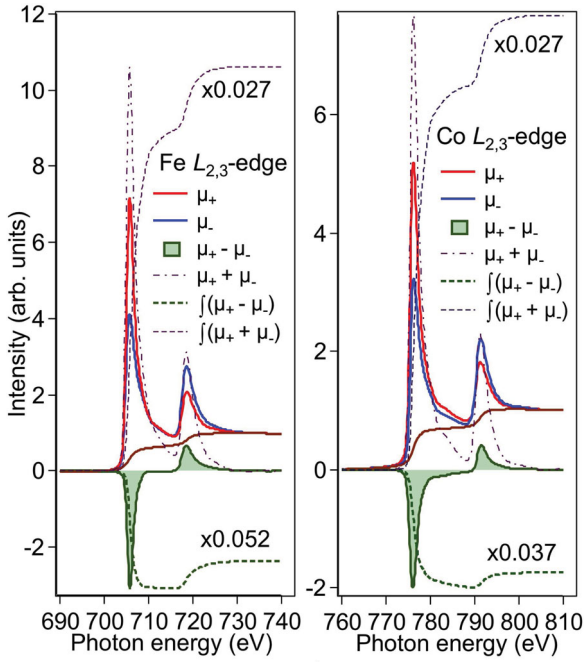

Figure 6. Sum rule analysis of normalized Co- and Fe $L_{2,3}$-edge XMCD spectra of annealed CoFeB/HOPG. The measurements were taken at remanence and at RT. The symbols shown in the figure are explained in the text.

and orbital magnetic moments[35–38] of Co and Fe in CoFeB/HOPG. **Figure 6** shows the Co and Fe $L_{2,3}$-edge XAS and XMCD spectra of an annealed 5 nm CoFeB film. The spectra have been corrected for the photon incident angle of 45° and the 75% degree of circular polarization, by multiplying the difference spectra by [1/cos(45°)]/0.75 while keeping the sum spectra unchanged. It is unambiguous that both of these elements in the film are free from oxidation and display very strong dichroic signals. The XMCD sum rules were applied to extract the spin and orbital magnetic moments of Co and Fe from the spectra.[37,39] Following the procedure established by Chen et al.,[36] the contributions of the continuum states were simulated by a two-step background function and subtracted from the absorption spectra for computing the 2p to 3d XAS intensities μ+ and μ_- for parallel and antiparallel alignment of photon helicity and magnetization.[36] The orbital- m_{orb} and spin magnetic moments m_{spin} were obtained from the integrals of the summed XAS $\int(\mu_+ + \mu_-)$ and XMCD $\int(\mu_+ - \mu_-)$ spectra for calculating the values for p, q and r,[36] using the following sum rules:

$$m_{orb} = -4q\,n_h/3r \quad (1)$$

$$m_{spin} = (4q - 6p)\,n_h/r \quad (2)$$

The number of holes n_h was taken as 2.49 for Co, and 3.39 for Fe.[36] The results of the sum rule analysis, compared to the bulk values, are summarized in **Table 2**. As shown, m_{spin} of Co and Fe are, respectively, 1.59 ± 0.20 and 2.00 ± 0.26 μ_B, both representing the bulk-like values.[36] On the other hand, the anomalously high q values obtained from the XMCD integrals

Table 2. Spin and orbital magnetic moments in units of μ_B per atom of CoFeB/HOPG, hcp-Co and bcc-Fe.

	$m_{orb}[\mu_B]$	$m_{spin}[\mu_B]$	m_{orb}/m_{spin}
Co in CoFeB/HOPG	0.661 ± 0.085	1.59 ± 0.20	0.416 ± 0.054
Fe in CoFeB/HOPG	0.543 ± 0.070	2.01 ± 0.26	0.271 ± 0.035
hcp-Co[36]	0.153	1.55	0.099
bcc-Fe[36]	0.086	1.98	0.043

for both edges give a remarkably high m_{orb} of 0.661 ± 0.085 and 0.543 ± 0.070 for Co and Fe of the annealed CoFeB film, respectively. With respect to bulk Co and Fe, these values imply an extraordinary enhancement of m_{orb} by 432% for Co and 631% for Fe. The orbital moments in itinerant ferromagnets are generally very weak due to the strong crystal-field perturbation of the 3d electron wave functions. Therefore, the observation of sizeable orbital moments in this alloy is surprising. In addition, the spectra show a substantial XMCD signal in between the two absorption edges, in particular at the Co L-edge, which has been previously attributed to "diffuse magnetism", involving s-electronic states instead of 3d electrons.[35,40,41] To harness the effects of such a diffuse part of the magnetic moments due to sp contributions in Ni and Co films, O'Brien and Tonner used a simplified atomic model similar to that introduced by Erskine and Stern,[42] and concluded that the diffuse magnetic moments have only little effect on the m_{spin} extracted from the XMCD sum rules.[34] In contrast, the m_{orb} computed using the same sum rule procedure could suffer from a large uncertainty as much as 25%.[35] In order to rule out the uncertainty introduced by the values of n_h, which are usually difficult to obtain from experiments, and the systematic error arising from the value of r, we compared the orbital-to-spin ratios m_{orb}/m_{spin} with those of bulk Co and Fe. The ratio for the Co in the alloy film is considerably larger than the Co bulk value, and, from a similar evaluation, the m_{orb}/m_{spin} of Fe is also much larger than that of bulk Fe.

In magnetic thin films, a reduction of symmetry at surfaces and interfaces, which can change the orbital degeneracy, could lead to an enhancement in the orbital moment. First-principles calculations on bcc-Fe surfaces have predicted a 100% enhancement of orbital moment as compared to the bulk value.[43] However, such an argument seems to be unlikely to explain our observation of a giant enhancement of about 631%. Since the total-electron-yield (TEY) signal mostly originates from the upper surface of the annealed CoFeB film, instead of the interface with graphite, the presence of B and boron oxide at the surface might play a role.

A very recent XMCD study of ultrathin (1 to 3 nm) CoFeB/MgO bilayers, which show a perpendicular magnetic anisotropy, has revealed similarly large m_{orb}/m_{spin}, with the authors suggesting its origin as magnetostriction.[44] On the other hand, it is well established that the presence of structural features, such as surface roughness, steps, or terraces, will lead to more localized atomic-like 3d wave functions and thus an enhanced orbital moment.[38] To explicitly confirm the origin of the unusual magnetic features found in the CoFeB thin films, further investigations with scanning tunneling microscopy, high-resolution transmission electron microscopy and X-ray spectroscopy would be necessary.

3. Conclusions

In summary, we have introduced a viable approach to fabricate crystalline FM/graphite interfaces by solid phase epitaxy of a-FM. With CoFeB, the particular ferromagnetic alloy being studied in this case, the obtained structural and electronic properties by a wide range of techniques suggest that the prerequisite requirements for the crystalline CoFe(110)/graphite interface as a spin filter can hardly be fulfilled, which has been ascribed as a consequence of the rather weak interaction and poor lattice match between CoFe(110) and graphite(0001) planes. Nevertheless, our study serves as a proof of principle that solid state epitaxy is a viable route towards engineering lattice matched ferromagnet/graphite-or-graphene interfaces, which is an important step forward. This is strengthened by the absence of B accumulation at the hybrid interface, which would otherwise break the favorable conditions for the spin-filtering effect. We expect that the same approach may be used to achieve films with a different texture. XMCD measurements and sum rule analysis show a bulk-like spin moment for both Co and Fe in the crystallized film. Surprisingly, sizeable orbital magnetic moments, in which a strong contribution by diffuse magnetism is apparent, have been observed, and its origin cannot be fully explained at present. We are convinced that this study should lead to a better knowledge as well as further investigations involving a-FM for carbon-based spintronic applications.

4. Experimental Section

CoFeB films on graphite were deposited in an ultrahigh vacuum chamber by e-beam evaporation of a $Co_{72}Fe_{20}B_8$ alloy source. Either an Al_2O_3 or BN crucible was used to accommodate the material. During the deposition, the chamber pressure was maintained below 8×10^{-10} mbar. The graphite substrates (highly oriented pyrolytic graphite, HOPG, Grade SPI–1, $10 \times 10 \times 1$ mm), were cleaved in situ in the load-lock chamber in order to minimize surface contaminations that could significantly affect and deteriorate the structural and magnetic properties of the deposited magnetic layer.[18,19,45]

The CoFeB/HOPG samples for PES and XAS measurements were prepared in situ at the experimental station of beam line D1011 (with a base pressure of 10^{-10} mbar) of MAX-Laboratory in Lund, Sweden. The XAS spectra were collected in total-electron-yield mode, where the sample drain current was recorded as a function of photon energy. To perform XMCD measurements, we used 75% left or right circularly polarized X-rays, which were incident at an angle of 45° with respect to the sample normal. To crystallize the as-deposited film for the XMCD measurements at remanence, the samples were annealed in vacuum at 400 °C for 60 min in the presence of a magnetic field of ≈0.1 T along the X-ray propagation direction using a permanent magnet. The XMCD signals were obtained by taking the difference in the absorption intensity measured for the left- and right helicity of the X-ray beam.

The surface structure at different stages of the in situ preparation was monitored by low-energy electron diffraction (LEED), while the film crystallinity was analyzed ex situ by XRD with Cu-Kα radiation. The B depth distribution in the samples was evaluated by ex situ sputtering XPS measurements. In-plane crystallinity of annealed CoFeB with respect to that of HOPG was studied by TEM and SAED measurements.

Supporting Information

Supporting Information is available from the Wiley Online Library or from the author.

Acknowledgements

The research leading to these results has received funding from the European Commission Seventh Framework Programme (FP7/2007-2013) under Grant Agreement number 228424 Project MINOTOR, the European Research Council (ERC Starting Grant no. 280020), and the NWO VIDI program, grant no. 10246.

Received: November 22, 2012
Published online: April 15, 2013

[1] W. J. M. Naber, S. Faez, W. G. van der Wiel, *J. Phys. D: Appl. Phys.* **2007**, *40*, R205.
[2] V. A. Dediu, L. E. Hueso, I. Bergenti, C. Taliani, *Nat. Mater.* **2009**, *8*, 707.
[3] D. Huertas-Hernando, A. Brataas, *Phys. Rev. B* **2006**, *274*, 155426.
[4] B. Trauzettel, D. V. Loss, G. Burkard, *Nat. Phys.* **2007**, *3*, 192.
[5] K. S. Novoselov, Z. Jiang, Y. Zhang, S. V. Morozov, H. L. Stormer, U. Zeitler, J. C. Maan, G. S. Boebinger, P. Kim, A. K. Geim, *Science* **2007**, *315*, 1379.
[6] C. Berger, Z. Song, X. Li, X. Wu, N. Brown, C. Naud, D. Mayou, T. Li, J. Hass, A. N. Marchenkov, E. H. Conrad, P. N. First, W. A. de Heer, *Science* **2006**, *312*, 1191.
[7] K. S. Novoselov, A. K. Geim, S. V. Morozov, D. Jiang, M. I. Katsnelson, I. V. Grigorieva, S. V. Dubonos, A. A. Firsov, *Nature* **2005**, *438*, 197.
[8] N. Tombros, C. Jozsa, M. Popinciuc, H. T. Jonkman, B. J. van Wees, *Nature* **2007**, *448*, 571.
[9] C. Jozsa, M. Popinciuc, N. Tombros, H. T. Jonkman, B. J. van Wees, *Phys. Rev. Lett.* **2008**, *100*, 236603.
[10] W. Han, W. H. Wang, K. Pi, K. M. McCreary, W. Bao, Y. Li, F. Miao, C. N. Lau, R. K. Kawakami, *Phys. Rev. Lett.* **2009**, *102*, 137205.
[11] W. Han, K. Pi, K. M. McCreary, Y. Li, J. J. I. Wong, A. G. Swartz, R. K. Kawakami, *Phys. Rev. Lett.* **2010**, *105*, 167202.
[12] A. Avsar, T. Y. Yang, S. K. Bae, J. Balakrishnan, F. Volmer, M. Jaiswal, Y. Zheng, S. R. Ali, G. Guntherodt, B.-H. Hong, B. Beschoten, B. Ozyilmaz, *Nano. Lett.* **2011**, *11*, 2363.
[13] T. Maassen, F. K. Dejene, M. H. D. Guimaraes, C. Jozsa, B. J. van Wees, *Phys. Rev. B* **2011**, *83*, 115410.
[14] J. -H. Chen, C. Jang, S. Xiao, M. Ishigami, M. S. Fuhrer, *Nat. Nanotechnol.* **2008**, *3*, 206.
[15] K. I. Bolotin, K. J. Sikes, Z. Jiang, M. Klima, G. Fudenburg, J. Hone, P. Kim, H. L. Stormer, *Solid State Commun.* **2008**, *146*, 351.
[16] V. M. Karpan, G. Giovannetti, P. A. Khomyakov, M. Talanana, A. A. Starikov, M. Zwierzycki, J. van den Brink, G. Brocks, P. J. Kelly, *Phys. Rev. Lett.* **2007**, *99*, 176602.
[17] M. Baumer, J. Libuda, H.-J. Freund, *Surf. Sci.* **1995**, *327*, 321.
[18] S. W. Poon, J. S. Pan, E. S. Tok, *Phys. Chem. Chem. Phys.* **2006**, *8*, 3326.
[19] P. K. J. Wong, M. P. de Jong, L. Leonardus, M. H. Siekman, W. G. van der Wiel, *Phys. Rev. B* **2011**, *84*, 054420.
[20] R. Hasegawa, *Glassy Metals: Magnetic, Chemical and Structural properties*, CRC Press, Boca Raton, FL, USA **1983**.
[21] D. Djayaprawira, K. Tsunekawa, M. Nagai, H. Maehara, S. Yamagata, N. Watanabe, S. Yuasa, Y. Suzuki, K. Ando, *Appl. Phys. Lett.* **2005**, *86*, 092502.
[22] Y. M. Lee, J. Hayakawa, S. Ikeda, F. Matsukura, H. Ohno, *Appl. Phys. Lett.* **2007**, *90*, 212507.
[23] W. H. Butler, X.-G. Zhang, T. C. Schulthess, J. M. MacLaren, *Phys. Rev. B* **2001**, *63*, 054416.
[24] T. Egami, *Rep. Prog. Phys.* **1984**, *47*, 1601.
[25] A. B. Preobrajenski, A. S. Vinogradov, E. Kleimenov, A. Knop-Gericke, S. A. Krasnikov, R. Szargan, N. Mårtensson, *Phys. Scripta* **2005**, *T115*, 1071.

[26] Y. Han, J. Han, H. J. Choi, H. -J. Shin, J. Hong, *J. Mater. Chem.* **2011**, *21*, 14967.
[27] *CRC Handbook of Chemistry and Physics* (Ed: D. R. Lide), CRC Press, Boca Raton, FL, USA **2009**.
[28] C. T. Campbell, *Surf. Sci. Rep.* **1997**, *28*, 1.
[29] P. V. Paluskar, J. J. Attema, G. A. de Wijs, S. Fiddy, E. Snoeck, J. T. Kohlhepp, H. J. M. Swagten, R. A. de Groot, B. Koopmans, *Phys. Rev. Lett.* **2008**, *100*, 057205.
[30] S. Yuasa, T. Nagahama, A. Fukushima, Y. Suzuki, K. Ando, *Nat. Mater.* **2004**, *3*, 868.
[31] J. D. Burton, S. S. Jaswal, E. Y. Tsymbal, O. N. Mryasov, O. G. Heinonen, *Appl. Phys. Lett.* **2006**, *89*, 142507.
[32] R. C. O'Handley, *Modern Magnetic Materials: Principles and Applications*, John Wiley & Sons, New York, NY, USA **2000**.
[33] T. Takeuchi, K. Tsunekawa, Y.-S. Choi, Y. Nagamine, D. D. Djayaprawira, A. Genseki, Y. Hoshi, Y. Kitamoto, *Jpn. J. Appl. Phys.* **2007**, *46*, L623.
[34] M. Talanana, *Ph.D Thesis*, University of Twente, the Netherlands **2006**.
[35] W. L. O'Brien, B. P. Tonner, *Phys. Rev. B* **1994**, *50*, 12672.
[36] C. T. Chen, Y. U. Idzerda, H.-J. Lin, N. V. Smith, G. Meigs, E. Chaban, G. H. Ho, E. Pellegrin, F. Sette, *Phys. Rev. Lett.* **1995**, *75*, 152.
[37] B. T. Thole, P. Carra, F. Sette, G. van der Laan, *Phys. Rev. Lett.* **1992**, *68*, 1943.
[38] G. van der Laan, *Phys. Rev. Lett.* **1999**, *82*, 640.
[39] P. Carra, B. T. Thole, M. Altarelli, X. D. Wang, *Phys. Rev. Lett.* **1993**, *70*, 694.
[40] S. S. Dhesi, H. A. Durr, G. van der Laan, E. Dudzik, N. B. Brookes, *Phys. Rev. B* **1999**, *60*, 12852.
[41] O. Eriksson, A. M. Boring, R. C. Albers, G. W. Fernando, B. R. Cooper, *Phys. Rev. B* **1992**, *45*, 2868.
[42] J. L. Erskine, E. A. Stern, *Phys. Rev. B* **1975**, *12*, 5016.
[43] O. Isnard, S. Miraglia, D. Fruchart, C. Giorgetti, S. Pizzini, E. Dartyge, G. Krill, J. P. Kappler, *Phys. Rev. B* **1994**, *49*, 15692.
[44] R. Knut, *Ph.D Thesis*, Uppsala University, Sweden **2012**.
[45] G.-X. Zhang, D. Q. Yang, E. Sacher, *J. Phys. Chem. C* **2007**, *111*, 17200.